CrystEngComm

Syntheses, Crystal Structures and Photocatalytic Properties of Four Hybrid Iodoargentates with Zero and Two-Dimensional Structures

Journal:	*CrystEngComm*
Manuscript ID	CE-ART-08-2015-001669.R2
Article Type:	Paper
Date Submitted by the Author:	20-Nov-2015
Complete List of Authors:	Lei, Xiao-Wu; Jining University, Department of Chemistry and Chemical Engineering Yue, Cheng-Yang; Jining University, Department of Chemistry and Chemical Engineering Feng, Li-Juan; Jining University, Department of Chemistry and Chemical Engineering Han, Yong-Fang; Jining University, Department of Chemistry and Chemical Engineering Meng, Rong-Rong; Jining University, Department of Chemistry and Chemical Engineering Yang, Jiang-Tao; Jining University, Department of Chemistry and Chemical Engineering Ding, Hao; Jining University, Department of Chemistry and Chemical Engineering Gao, Chuan-Sheng; Jining University, Department of Chemistry and Chemical Engineering Wang, Chun-Yan; Jining University, Department of Chemistry and Chemical Engineering

Syntheses, Crystal Structures and Photocatalytic Properties of Four Hybrid Iodoargentates with Zero and Two-Dimensional Structures

Xiao-Wu Lei,[a,*] Cheng-Yang Yue, [a,b,c*] Li-Juan Feng,[a] Yong-Fang Han,[a] Rong-Rong Meng,[a] Jiang-Tao Yang,[a] Hao-Ding,[a] Chuan-Sheng Gao,[a] Chun-Yan Wang[a]

[a]Key Laboratory of Inorganic Chemistry in Universities of Shandong, Department of Chemistry and Chemical Engineering, Jining University, Qufu, Shandong, 273155, China

[b]State Key Laboratory of Structural Chemistry, Fujian Institute of Research on the Structure of Matter, Chinese Academy of Sciences, Fuzhou 350002, P. R. China

[c]Collaborative Innovation Center of Chemistry for Energy Materials (iChEM), Xiamen University, Xiamen, Fujian 361005, P. R. China

**Corresponding author*: Xiao-Wu Lei, Cheng-Yang Yue

E-mail address: xwlei_jnu@163.com; yuechengyang@126.com

Abstract: With $[TM(phen)_3]^{2+}$ (TM = transition metal, phen = 1,10-phenanthroline) complex and N-alkylated $[(Me)_2$-2,2'-bipy$]^{2+}$ (Me = methyl, 2,2'-bipy = 2,2'-bipyridine) as cations, a series of hybrid iodoargentates, namely, $[TM(phen)_3]_2Ag_3I_7$ (TM = Mn (**1**), Fe (**2**)), $[Mn(phen)_2]Ag_5I_7$ (**3**) and $[(Me)_2$-2,2'-bipy$]_2Ag_7I_{11}$ (**4**), have been solvothermally prepared and structurally characterized. Compounds **1**-**2** feature isolated windmill-shaped $[Ag_3I_7]^{4-}$ trimers based on $[AgI_3]$ triangles, whereas compound **3** contains two-dimensional (2D) microporous $[Ag_5I_7]^{2-}$ layers composed of $[Ag_3I_7]$ and $[Ag_7I_{13}]$ secondary building units (SBUs) based on $[AgI_4]$ tetrahedra. In compound **4**, the 2D $[Ag_7I_{11}]^{4-}$ slab is formed by alternating interconnection of two different types of $[Ag_7I_{12}]$ double chains via corner-sharing with one-dimensional (1D) large channels occupied by the $[(Me)_2$-2,2'-bipy$]^{2+}$ cations. The UV-vis diffuse-reflectance measurements reveal that the title compounds possess semiconductor behaviors with smaller band gaps of 1.85, 1.78, 1.89 and 2.03 eV, respectively. Sample **4** shows highly efficient photocatalytic degradation activity over organic pollutant than N-doped TiO_2 (P25) under visible light irradiation. Moreover, a possible mechanism for the stable photocatalytic activity is proposed based on band structure calculation. Finally, the luminescent properties and thermal stabilities of the title compounds are also studied.

Introduction

Inorganic-organic hybrid metal halides have attracted much attention in the past several decades owing to the fascinating anionic structural diversities and distinctive properties inheriting from the inorganic and organic components, as well as potential applications in many fields, such as semiconducting, luminescent, nonlinear optical, photochromic and thermochromic effects, etc.[1-6] Among these hybrid materials, the iodoargentates are especially attractive for their tunable structures due to the strong affinity of Ag(I) for I^- anion, myriad coordination geometries including linear AgI_2, triangle AgI_3 and tetrahedral AgI_4 units as well as the semiconducting properties.[7-15] More interestingly, the tetrahedral AgI_4 unit features high self-assembly characterization and diversiform condensation modes including corner-, edge- and face-sharing as well as weak Ag···Ag interaction, termed argentophilicity.[8] Up to now, many iodoargentate anionic networks with the general formula of $(Ag_mI_n)^{(n-m)-}$ have been synthesized and structurally characterized, such as zero-dimensional (0D) clusters of $[Ag_4I_8]^{4-}$, $[Ag_5I_9]^{4-}$, $[Ag_5I_{10}]^{5-}$, $[Ag_6I_{12}]^{6-}$, $[Ag_7I_{13}]^{6-}$;[7,9,10] 1D chains of $[AgI_2]^-$, $[Ag_2I_5]^{3-}$, $[Ag_4I_6]^{2-}$, $[Ag_5I_7]^{2-}$, $[Ag_6I_8]^{2-}$;[11-17] 2D layers of $[Ag_2I_3]^-$, $[Ag_4I_5]^-$, $[Ag_5I_6]^-$, $[Ag_{11}I_{15}]^{4-}$ and three-dimensional (3D) frameworks of $[AgI_2]^-$, $[Ag_4I_6]^{2-}$, $[Ag_5I_7]^{2-}$, etc.[18-19] In the assembly process of anionic iodoargentate networks, the organic cations play one of the most important internal factors although some external factors including pH value, solvent and reaction temperature also play indispensable roles. Hence, an effective strategy for the rational design of valuable iodoargentate networks is to introduce proper organic cations into the hybrid iodoargentates.

On the other hand, the functional hybrid has became more and more important in the rational design of hybrid materials based on band structure design in addition to the crystal engineering, because that the band structure belongs to the essential factor of photoelectric semiconductors. Recently, it is found that the band structures of hybrid iodoargentates can be regulated by selecting proper organic cations. For example, the aliphatic organic cations of $(H_2pipe)^{2+}$ (pipe = piperazine) and $(Me_2teda)^{2+}$ (teda = triethylenediamine) lead to the blue shifts of absorption edges for $(H_2pipe)_{0.5}(\alpha\text{-}AgI_2)$ and $(Me_2teda)_{0.5}(\alpha\text{-}AgI_2)$, whereas the conjugated $(H_2dpe)^{2+}$ (dpe = 1,2-di(4-pyridyl)ethylene) leads to the

red shift of $(H_2dpe)_{0.5}(\beta\text{-}AgI_2)$ comparing with the β-AgI.[11a] As a matter of course, incorporation of suitable functional organic cations in the controllable syntheses of hybrid iodoargentates has been proved to be a valuable strategy based on not only crystal engineering but also band structure design. Comparing with the frequently-used organic cations, such as alkylammonium or aliphatic amine, multi-pyridine derivatives feature excellent electron accepting abilities and have been widely applied in the photoelectric materials. Furthermore, these multi-pyridine derivatives are able to not only chelate the TM ions to form complex cations but also be *in situ* N-alkylated into new organic cations. Especially, the TM complex cations may enhance or improve the electronic, optical and magnetic properties of hybrid materials arriving from the abundant *d* orbital electrons. But until now, only few TM complex cations directed iodoargentates were reported comparing with those based on organic cations, for example $[Ni(2,2'\text{-bipy})(THF)_2(H_2O)_2](Ag_{10}I_{12})\cdot 2DMF$, $[Cu(2,2'\text{-bipy})_3]Ag_5I_7$, $[Mn(4,4'\text{-bipy})(DMSO)_4]_2Ag_{11}I_{15}$, etc.[20-21]

Intrigued by the diverse structural topologies and potential photoelectric behaviors of these hybrid materials, we undertook systematic studies in the hybrid iodoargentates based on multi-pyridine derivatives. Here, we adopted *in situ* generated $[TM(phen)_3]^{2+}$ complex and $[(Me)_2\text{-}2,2'\text{-bipy}]^{2+}$ as cations leading to four new hybrid iodoargentates, namely, $[TM(phen)_3]_2Ag_3I_7$ (TM = Mn, Fe), $[Mn(phen)_2]Ag_5I_7$ and $[(Me)_2\text{-}2,2'\text{-bipy}]_2Ag_7I_{11}$. The UV-vis diffuse-reflectance measurements reveal that the compounds possess proper semiconducting behaviors and visible light absorption, which lead to the highly efficient heterogeneous photocatalytic activity under visible light irradiation for compound **4**. Herein, we report their syntheses, crystal structures, band structures and photocatalytic properties.

Experimental Section

Materials and Methods All analytical grade chemicals employed in this study were commercially available and used without further purification. N-doped TiO_2 (P25) was synthesized following the previously reported method, that is, by treating commercially available TiO_2 in the NH_3 (67%)/Ar atmosphere at 550°C for 10 hours.[22] Elemental analyses were performed using a German Elementary

Vario EL III instrument. The solid state UV−vis spectra were measured at room temperature using a PE Lambda 900 UV/vis spectrophotometer in the wavelength range of 200−800 nm. Thermogravimetric analyses were carried out with a Mettler TGA/SDTA 851 thermal analyzer under N_2 atmosphere with a heating rate of 10 °C·min^{-1}. The photoluminescence measurements were carried out on a FLS920 fluorescence spectrophotometer equipped with a continuous Xe-900 xenon lamp and a μF900 microsecond flash lamp.

Syntheses of Compounds 1-2. A mixture of KI (1.5 mmol), $Mn(CH_3COO)_2$•$4H_2O$ (0.5 mmol), AgI (1 mmol), phen (1.5 mmol), hydroiodic acid (1 mL) and acetonitrile (4 mL) was sealed in a 15-mL Teflon-lined stainless container, which was heated at 140 °C for 6 days, and then cooled to room temperature. The product contained block-shaped dark red crystals of **1** (yield: 27% based on Ag) and indefinite yellow powder. The crystals of **1** were selected by hand, washed with distilled water and ethanol, and then dried in the air. Elem. Anal. Calcd for $C_{72}N_{12}H_{48}Mn_2Ag_3I_7$ (**1**): C, 35.98%; H, 2.01%; N, 6.99 %; found: C, 35.90%; H, 1.91%; N, 7.09 %. Compound **2** was synthesized in the analogous manner to that of **1** with $FeSO_4$•$7H_2O$ instead of $Mn(CH_3COO)_2$•$4H_2O$. The dark red crystals of **2** were obtained in yield of 25% based on Ag. Elem. Anal. Calcd for $C_{72}N_{12}H_{48}Fe_2Ag_3I_7$ (**2**): C, 35.96%; H, 2.01%; N, 6.99 %; found: C, 35.88%; H, 2.09%; N, 6.95 %.

Synthesis of Compound 3. The mixture of KI (1 mmol), $Mn(CH_3COO)_2$•$4H_2O$ (0.5 mmol), phen (1.5 mmol), AgI (3 mmol), hydroiodic acid (1 mL) and acetonitrile (4 mL) was sealed in a 15-mL Teflon-lined stainless container, which was heated at 140 °C for 6 days, and then cooled to room temperature. The product contained dark red crystals of **3** and some yellow powder. The crystals were selected by hand, washed with distilled water and ethanol, and then dried in the air. The yield of the compound **3** is 0.158 g (13%) based on Ag. Elem. Anal. Calcd $C_{36}N_6H_{24}MnAg_5I_7$ (**3**): C 21.37%, H 1.19%, N 4.15 %. Found: C 21.28%, H 1.29%, N 4.26 %.

Synthesis of Compound 4. Mixture of KI (2 mmol), 2,2'-bipy (0.5 mmol), AgI (4 mmol), HI aqueous solution (1.0 mL), and methanol (4.0 mL) was sealed in a stainless steel reactor, and then was reacted on the same condition as those of compounds **1**-**3**. Subsequently, orange-red crystals of **4** were obtained and

washed with ethanol with yield of 35% based on Ag. Elem. Anal. Calcd for $C_{24}N_4H_{28}Ag_7I_{11}$: C, 11.42%, H, 1.12%, N, 2.22 %; found: C, 11.33%, H, 1.23%, N, 2.17 %.

Crystallographic Studies. Single crystals of the title compounds were collected on a Bruker SMART CCD-based diffractometer (Mo Kα radiation, λ = 0.71073 Å) at room temperature. The absorption corrections were applied using a multi-scan technique. The structures of title compounds were solved by direct method and refined by full-matrix least-square on F^2 using the SHELXL-97 program.[23] All non-hydrogen atoms were refined with anisotropic thermal parameters, and the hydrogen atoms of organic molecules were generated theoretically onto the carbon atoms and refined isotropically with fixed thermal factors. In compound **4**, the Ag(1), Ag(2) and Ag(6) atoms featured slightly disorder over two positions with refined occupancies of 0.84(7), 0.80(4), 0.80(7) for Ag(1a) Ag(2a) and Ag(6a) positions, respectively. Hence, these atoms will be used to discuss the crystal structure in this paper. The crystallographic data for all the compounds are listed in Table 1 and important bond lengths are listed in Tables S1-S3. More details on the crystallographic studies are given in Supporting Information.

Calculation Detail. The density of state (DOS) of compound **4** was calculated by density functional theory (DFT) using the crystallographic data with the CASTEP code, which used a plane-wave basis set for the valence electrons and norm-conserving pseudopotential for the core electrons.[24] The number of plane waves included in the basis were determined by a cutoff energy of 320 eV. Pseudoatomic calculations were performed for Ag-4$d^{10}5s^1$, I-5$s^2$5p^5, C-2$s^2$2p^2, N-2$s^2$2p^3 and H-1s^1. Other calculating parameters and convergence criteria were set by the default values of the CASTEP code, for example, an energy convergence tolerance of 1.0×10^{-5} eV.

Powder X-ray diffraction. The powder X-ray diffraction (PXRD) patterns of the ground powder of **1**–**4** were collected at room temperature on a X'Pert-Pro diffractometer using Cu Kα radiation (λ = 1.5406 Å) in the 2θ range of 5–80°. PXRD patterns were in good agreement with the simulated patterns generated using the CIF documents of each refined structure (Fig. S6). The broad peaks mainly originated from the excessively small amount of experimental sample. Furthermore, inferior crystal

qualities and relative larger particle sizes of the powder also decreased the measurement accuracies. However, this did not affect the results of subsequent physical properties.

Photocatalytic Activity Measurements. The photocatalytic activity of as-prepared sample **4** was evaluated by the degradation of Crystal Violet (CV) and Rhodamine B (RhB) as model dye pollutants under visible light irradiation from a 50 W Xe lamp. The cut-off filter was used to remove all wavelengths less than 400 nm and more than 780 nm ensuring irradiation with visible-light only. In a typical process, 30 mg sample **4** was added to a 30 mL of 4×10^{-5} mol·L^{-1} solution of CV and RhB, respectively, and the mixture was magnetically stirred in the dark for 10 hours to ensure adsorption equilibrium between the catalyst and solution before irradiation, and then the solution was exposed to visible light irradiation. After a given irradiation time, 4 mL of the mixture was continually taken from the reaction cell and the catalyst was separated from the suspension by high-speed centrifugation. The temporal changes of concentration for CV and RhB solution were monitored by examining the intensities of the maximal absorption at 589 and 552 nm in UV-Vis spectra, respectively.

Results and Discussion

Syntheses Aspects. Compounds **1**-**3** were solvothermally synthesized in the mixed solvent of HI and acetonitrile, whereas compound **4** was obtained in HI and ethanol solution. In the syntheses of compounds **1**-**3**, the dosage ratio of transition metal and AgI played key role due to the nearly same reaction conditions. The low ratio will led to the formation of compounds **1**-**2**, and high one resulted in the produce of compound **3**, which was also in agreement with their chemical compositions. In the solvothermal reaction, the TM ions were *in situ* chelated by phen ligands into $[TM(phen)_3]^{2+}$ complex cations, and $[(Me)_2$-2,2'-bipy$]^{2+}$ cations was also *in situ* generated due to the acidic environment. The similar *in situ* reactions had also been reported in many inorganic-organic materials.[25-26] Furthermore, the KI was added in the reaction not only used as the source of I^- but also effectively increase the solubility of AgI, which played a very important role in the formation of the title compounds.

Crystal Structures

Structures of $[TM(phen)_3]_2Ag_3I_7$ (TM = Mn (1), Fe (2)). Single-crystal X-ray diffraction analyses revealed that compounds **1**−**2** belong to the isostructural phases. Hence, compound **1** is taken as the example to depict their crystal structures. In the asymmetric unit of compound **1**, there is one crystallographically independent Mn^{2+} ion, one Ag^+ ion, two I^- ions as well as one phen ligand. The Ag(1) ion is coordinated by three I^- ions with a planar $[AgI_3]$ triangle coordination environment with I-Ag-I angles of 122.78(4)º and 118.61(2)º. The Ag-I bond distances of 2.7266(7)-2.8755(9) Å are comparable with those of reported hybrid iodoargentates, such as $[HCP]Ag_2I_3$, $[MC]Ag_2I_3$, etc.[18,19] Relatively speaking, the planar $[AgI_3]$ triangle is seldom founded in hybrid iodoargentates comparing with the $[AgI_4]$ tetrahedron.[27] Three $[AgI_3]$ units are self-condensed via sharing one terminal I(1) atom to form an isolated $[Ag_3I_7]^{4-}$ trimer (Fig. 1a). It should be noted that three $[AgI_3]$ triangles do not locate at the same plane in $[Ag_3I_7]^{4-}$ trimer but feature a windmill shape with dihedral angle of 43.89º. The neighboring $[Ag_3I_7]^{4-}$ trimers feature parallel stacking model along the *a*- and *b*-axis in an approximate plane, which is separated by the $[Mn(phen)_3]^{2+}$ complex cations along the *c*-axis (Fig. 1c).

Structure of $[Mn(phen)_3]_2Ag_5I_7$ (3). Compound **3** crystallizes in the triclinic space group *P*-1 (No. 2). The asymmetric unit consists of two crystallographically independent Mn^{2+}, ten Ag^+, fourteen I^- ions and six phen ligands. All the Ag^+ ions are coordinated by four I atoms with slightly distorted tetrahedral environments. The Ag-I bond distances fall in the range of 2.7687(13)-2.9980(15) Å, which are according with those of AgI_4 tetrahedra in other hybrid iodoargentates, such as $Zn(en)_3Ag_2I_4$, $[HCP]Ag_2I_3$, $[MC]Ag_2I_3$, $[BPB]Ag_5I_7$, etc.[7b,18-20] As shown in Fig. 2a, each $Ag(7)I_4$, $Ag(9)I_4$ and $Ag(10)I_4$ tetrahedron is condensed via edge-sharing to form a triangular $[Ag_3I_7]$ trimer with three outside I(1) atoms, which is similar to the $[Cu_3I_7]$ unit in $[De\text{-}DABCO]_2[Me\text{-}DABCO]Cu_{11}I_{17}$.[28] On the other hand, each Ag(1), Ag(2), Ag(3), Ag(4), Ag(6) and Ag(8) tetrahedron is interconnected via edge-sharing to form a cricoid $[Ag_6I_{13}]$ unit with one centered I(14) atom and three outside I atoms (Fig. 2b). The Ag(5) atom further cap the $[Ag_6I_{13}]$ unit via Ag-I bonds to form the $[Ag_7I_{13}]$ SBU, which has not been reported in hybrid iodoargentates until now. In the $[Ag_3I_7]$ and $[Ag_7I_{13}]$ SBUs, there are abundant weak Ag···Ag bonds of 2.7868(16)-3.3560(16) Å, which are shorter than the sum of the van der Waals radii of

Ag^{I} (3.44 Å), indicating the presence of weak argentophilic interactions.[29] The $[Ag_3I_7]$ trimers and $[Ag_7I_{13}]$ units as new SBUs are interconnected via sharing the terminal iodine atoms to form the novel 2D $[Ag_5I_7]^{2-}$ layer along the *ab*-plane with a (6,3) topological network (Fig. 2c). As a result, the 2D layer contains a $[Ag_9I_9]$ 18-membered ring with an approximate hexagonal cross-section of 6.834 ×9.677 $Å^2$ presented along the *c*-axis. In the 2D $[Ag_5I_7]^{2-}$ layer, each $[Ag_3I_7]$ trimer connects three $[Ag_7I_{13}]$ units and vice versa for each $[Ag_7I_{13}]$ unit, that is, both $[Ag_3I_7]$ and $[Ag_7I_{13}]$ unit act as three-connected nodes to form the 2D microporous $[Ag_5I_7]^{2-}$ layer. These 2D layers feature stacking arrangement in parallel mode along the *c*-axis and separated by the $[Mn(phen)_3]^{2+}$ complex cations (Fig. 2d).

It is worth noting that the tetrahedral $[AgI_4]$ unit often undergoes a variety of self-condensation to form polyanionic units including clusters or oligomers as SBUs, such as $[Ag_4I_8]^{4-}$, $[Ag_5I_9]^{4-}$, $[Ag_5I_{10}]^{5-}$, $[Ag_6I_{12}]^{6-}$, etc. However, most of the SBUs are self-condensed to form 1D anionic chains, such as $[Ag_4I_6]^{2-}$, $[Ag_5I_7]^{2-}$, $[Ag_6I_9]^{3-}$, $[Ag_8I_{12}]^{4-}$, $[Ag_{10}I_{12}]^{2-}$, $[Ag_{10}I_{14}]^{4-}$, etc.[11-17] Occasionally, these SBUs can also be interlinked to form 2D microporous layers, for example, 2D $[Ag_2I_3]^{-}$ and $[Ag_5I_8]^{3-}$ layers are composed of $[Ag_4I_8]^{4-}$ and $[Ag_5I_{10}]^{2-}$ SBUs with approximately quadrangular $[Ag_8I_8]$ and $[Ag_6I_6]$ rings, respectively.[18a,21a] Undoubtedly, the 2D $[Ag_5I_7]^{2-}$ reported here based on $[Ag_3I_7]$ and $[Ag_7I_{13}]$ building blocks represents a new microporous layer with large size pore in hybrid iodoargentate chemistry, which further indicates the unique structural directing effects of TM complex cations.

Structure of $[(Me)_2$-2,2'-bipy$]_2Ag_7I_{11}$ (4). Compound **4** crystallizes in the triclinic space group *P*-1 (No. 2) and presents a 2D $[Ag_7I_{11}]^{4-}$ slab directed by $[(Me)_2$-2,2'-bipy$]^{2+}$ cations. The asymmetric unit of **4** has 14 crystallographically independent Ag^{+} ions, 22 I^{-} ions and four $[(Me)_2$-2,2'-bipy$]^{2+}$ molecules. All the Ag^{+} ions are tetrahedrally coordinated by four iodine atoms with normal Ag-I bond distances of 2.7136(12)-3.1116(12) Å, which are close to those of compounds **1-3**. As shown in Fig. 3a, the 2D $[Ag_7I_{14}]^{7-}$ anionic slab is built from two different types of $[Ag_7I_{12}]$ double chains (marked as A and B types) interconnected via corner-sharing.

In the A-type $[Ag_7I_{12}]$ chain, each $Ag(1)I_4$, $Ag(2)I_4$, $Ag(7)I_4$, $Ag(10)I_4$ and $Ag(12)I_4$ tetrahedron is initially self-condensed via edge-sharing to form an open $[Ag_5I_{10}]$ unit, which is evidently different from the $[Ag_5I_{10}]$ SBU in $[Tb(DMSO)_8]_2[Ag_2I_5][Ag_5I_8]$.[21a] The neighboring $[Ag_5I_{10}]$ units are bridged by the $Ag(3)I_4$ tetrahedrons via sharing three outside iodine atoms (I(1), I(4) and I(13) atoms) to form a $[Ag_6I_{12}]$ single chain along the *a*-axis. At the other hand, two $Ag(8)I_4$ tetrahedra are aggregated into a $[Ag_2I_6]$ dimer, each of which bridge two parallel $[Ag_6I_{12}]$ single chains via sharing the four outside iodine atoms to form a ladder shaped $[Ag_7I_{12}]$ double chain along the *a*-axis. Such connectivity also leads to a large ring with an approximate quadrangular cross-section of 7.759 × 16.176 $Å^2$ presented along the *b*-axis. In the B-type $[Ag_7I_{12}]$ chain, each $Ag(4)I_4$, $Ag(5)I_4$, $Ag(6)I_4$, $Ag(9)I_4$ and $Ag(14)I_4$ tetrahedron also forms the same open $[Ag_5I_{10}]$ unit as that in A-type chain. But the neighboring $[Ag_5I_{10}]$ units are interlinked by $Ag(13)I_4$ tetrahedra in the opposite direction to that of A-type chain into another type of $[Ag_6I_{12}]$ single chain. Subsequently, such two parallel $[Ag_6I_{12}]$ chains are also bridged by the $[Ag_2I_6]$ dimers composed of two $Ag(11)I_4$ tetrahedra to form the B-type of $[Ag_7I_{12}]$ double chain, which also contains the large $[Ag_{12}I_{12}]$ ring with approximate quadrangular cross-section of 7.112 × 12.999 $Å^2$. These two different types of $[Ag_7I_{12}]$ double chains are interlinked via corner-sharing to form the 2D anionic $[Ag_7I_{11}]^{4-}$ slab in the *ab*-plane with 1D large tunnel among the A- and B-type double chains (Fig. 3a). There are also abundant weak Ag···Ag bonds with distances of 2.9658(17)-3.3323(14) Å, which are close to those of compound **3**. The 2D $[Ag_7I_{11}]^{4-}$ slabs feature parallel stacking along the *c*-axis, and the $[(Me)_2$-2,2'-bipy$]^{2+}$ cations occupy the 1D tunnels as well as the space among the slabs (Fig. 3b).

Thermal Stabilities Thermal stabilities of compounds **1**–**4** were investigated by the thermogravimetric analyses (TGA) under nitrogen atmosphere in the temperature range of 30–800 °C. As shown in Fig. S2, the TGA curves of compounds **1** and **2** feature the two-step weight loss of all phen lignads in the range of about 225-540 °C and 250-520 °C, respectively, with total weight losses of 50.05 % and 44.23 %, which are close to the theoretical values of 44.99 % and 44.96 %. Compound **3** starts to decompose at about 200 °C and do not achieve the balance until to 800 ºC, which may be due to

that the decomposition of complex cations simultaneously leads to the complete collapse and volatilization of the iodoargentate anionic networks. From about 180 to 300 °C, compound **4** has a one-step weight loss of 14.65 % (theoretical value of 14.76%), corresponding to the loss of all organic cations per formula. After the major weight loss, compound **4** continues to slowly lose weight at 650 ºC and does not achieve the balance to 800 ºC.

Optical Properties The solid-state optical diffuse reflection spectra of the compounds **1**-**4** were measured from powder samples at room temperature. The absorption spectra calculated from the diffuse reflectance data by using the Kubelka–Munk function are plotted in Fig. 4. Extrapolation of the linear portion of the absorption edges give the optical band gaps of 1.85, 1.78 and 1.89 eV for compounds **1**-**3**, respectively, which are accordance with their colors of dark red. The band gap of compound **4** is estimated as 2.03 eV corresponding to the orange-red color. The slightly larger band gap of **4** than those of compounds **1**-**3** mainly due to the different contributions of TM complexes and organic cations, respectively. Obviously, all the title compounds have smaller band gaps and exhibit red shifts of the absorption edge compared with the bulk *β*-AgI (2.81 eV), and similar red shifts have also been reported in some hybrid iodoargentates containing conjugated organic cations, such as $[HCP]Ag_2I_3$ (1.89 eV), $[MCP]Ag_4I_5$ (2.63 eV) and $(H_2dpe)Ag_2I_4$ (1.99), etc.[18a,11a]

The luminescent spectrums of the compounds **1**, **3** and **4** in solid state are investigated on crystalline samples at room temperature with the results shown in Fig. S3. When excited at 260 nm, compounds **1**, **3** and **4** give strong emissions with λ_{max} = 520, 570 and 600 nm, respectively. These luminescent properties are similar to those of hybrid iodoargentates, such as $[Ni(2,2'\text{-bipy})(THF)_2(H_2O)_2](Ag_{10}I_{12})\bullet 2DMF$ (447 and 518 nm), $(BPO)Ag_5I_7$ (569 nm), $(pql)Ag_2I_3$ (599 nm), $(npql)_2Ag_4I_6$ (563 and 614 nm), etc.[20b,7b,12a] In the structures of compounds **1**, **3** and **4**, there are not covalent bonds between the cations and iodoargentate skeletons. Hence, these emission bands can be assigned to the mixture of iodide(X)-to-metal charge transfer (XMCT) and metal centered states (Ag-5*s* or 5*p* to Ag-4*d*) modified by the weak Ag···Ag interactions, which have been investigated and proved by the molecular orbital calculations for some related hybrid iodoargentates.[30]

Photocatalytic Properties The narrow band gaps of compounds **1**-**4** encourages us to investigate the photocatalytic activities, which were evaluated by the degradation of CV and RhB as model dye pollutant under visible light irradiation at room temperature. Before the photocatalytic experiments, neither the photolysis experiment without photocatalyst nor the catalytic experiment without light irradiation showed any observable decrease in CV and RhB concentration with time. After the powder sample **4** was added to the solution of CV or RhB, the mixture was magnetically stirred in the dark for 10 hours to achieve absorption equilibrium between the photocatalyst and CV or RhB molecule. Under the visible light irradiation, the absorption spectra of residual CV and RhB solution gradually decrease with the increasing of reaction time, which is also demonstrated by the changes in the color of the solution (Fig. 6). Hence, the monotonic decrease of absorbance intensities indicates that the CV and RhB molecules are photodegraded by sample **4** under visible light illumination. Under the same conditions, samples **1**-**3** feature strong absorption or slightly photodegradation effects for CV and RhB, and only the photocatalytic activity of sample **4** was studied in detail.

The plots of C/C_0 of CV and RhB solutions versus irradiation time for compound **4** are given in Fig. 5, where C and C_0 represent the remnant and initial concentrations of organic dyes, respectively. Under the photodegradation action of sample **4**, the degradation ratio of CV reaches 94% exposed to the visible light irradiation for 30 min, and then achieves nearly 100% after 50 min resulting in complete decolorization (Fig. 5b). For RhB solution, sample **4** also shows evident photodegradation activity and about 95% of RhB is decomposed after visible light irradiation for 60 min (Fig. 5d). At the same time, we studied the photodegradation property of photocatalyst N-doped P25 for comparing under the completely same condition, and the results show that more than 71 % of CV and 62 % of RhB are still alive after irradiation for 60 min. Obviously, sample **4** features higher photodegradation activity than N-doped P25 for CV and RhB dye pollutant under visible light irradiation. To further accurately evaluate the photocatalytic activities of the sample **4** and N-doped P25, we study the kinetic process of photodegradation reaction by calculating the relationship between $\mathrm{Ln}(C_0/C)$ and reaction time. The results show that all the $\mathrm{Ln}(C_0/C)$ values follow the linear relationships over the reaction time, that is, all

the photodegradation process belong to the first-order kinetic reactions (Fig. S4a and S5a). The corresponding rate constants obtained from the linear fitted method of sample **4** (91×10^{-3} and 39×10^{-3} min^{-1}) are found to be 13.8 and 4.6 times larger than the N-doped P25 (6.6×10^{-3} and 8.3×10^{-3} min^{-1}) for CV and RhB, respectively. As recyclability for photocatalyst is a general requirement for potential application, cyclic experiments for CV and RhB were carried out, and the sample was collected after the first cycle usage to carry out subsequent degradation. It is found that there is only slight decrease of about 5% in the catalytic efficiency over three cycles, which is maybe due to the little loss of powder sample in the collection process (Fig. S4b and S5b). Finally, the XRD pattern of recovered sample after photodegradation is still in agreement with those of as-prepared sample as well as the simulated data, which indicates that the basic structure remain unchanged and sample **4** can be used as stable visible light responding photocatalyst for organic dye destruction (Fig. S5d). Similar photocatalytic effects have also been observed in some hybrid iodoargentates and iodocuprates directed by organic or transition metal complex cations, such as $[De\text{-}DABCO]_2[Me\text{-}DABCO]Cu_{11}I_{17}$, $[Co(phen)_3](Ag_3I_5)\cdot 2CH_3CN$, $[TM(phen)_3]_2Ag_{11}I_{15}\cdot H_2O$ (TM = Co, Cu), $[TM(phen)_3]_2Ag_{13}I_{17}$ (TM = Co, Cd), $(Hpy)Ag_2I_3$, $(Hpy)_2\cdot dmf\cdot Ag_6I_8$, $(Hpy)_2\cdot H_2O\cdot Ag_3I_5$, $(Hpy)Ag_5I_6$, $K[TM(2.2\text{-}bipy)_3]Ag_6I_{11}$ (TM = Mn, Fe, Co, Ni, Zn), $[TM(2,2\text{-}bipy)_2I]_2Cu_7I_9$ (TM = Mn, Cu) and $K[Mn(2,2\text{-}bipy)_3]_2Cu_6I_{11}$, etc.[28, 33]

The evident and stable photocatalytic activity for sample **4** requires an effect way of separating the electron-hole pair generated by visible light irradiation. Hence, we calculate the band structure of compound **4** based on the DFT method to gain insight the possible photocatalytic mechanism. As shown in Fig. 6, the valence band just below the Fermi level of compound **4** (the top of the valence band) is mainly contributed by the 5*p* state of I and the 4*d* state of Ag mixed with a little C-2*s* and -2*p* orbitals, and the conduction band just above the Fermi level in the range of 2.1-3.2 eV is mainly derived from the C-2*p* and N-2*p* orbitals. Therefore, the electron transition of compound **4** mainly occurs between the anionic 2D $[Ag_7I_{11}]^{4-}$ slabs and conjugated organic cations. In the typical photocatalytic process, the hybrid sample **4** can be excited to produce the electron-hole pairs under visible light irradiation. According to the band structure calculation, the holes move to the anionic $[Ag_7I_{11}]^{4-}$ slabs, and electrons

migrate to the conjugate $[(Me)_2\text{-}2,2'\text{-bipy}]^{2+}$ cations. The holes of anionic $[Ag_7I_{11}]^{4-}$ layers will correspond to the oxidation of I^- to alive I^0 atom, which is able to oxide the organic pollutants and hence become reduced to I^- ions again. In general, the photogenerated electrons of $[(Me)_2\text{-}2,2'\text{-bipy}]^{2+}$ cations are expected to be trapped by O_2 in the solution to form superoxide ions ($\cdot O_2^-$) and other reactive oxygen species.[31-32] Hence, the transfer of electrons to organic cations enables hybrid iodoargentate of $[(Me)_2\text{-}2,2'\text{-bipy}]Ag_7I_{11}$ to be more stable than AgI under irradiation because of the lower electron concentration in the 2D $[Ag_7I_{11}]^{4-}$ slabs.

Conclusion

In conclusion, a series of inorganic–organic hybrid iodoargentates based on TM complex and organic cations have been solvothermally synthesized, structurally and optically characterized. The prepared hybrid iodoargentate of $[(Me)_2\text{-}2,2'\text{-bipy}]Ag_7I_{11}$ display enhanced visible light absorption and excellent photodegradative ability for organic contaminant. The dramatic and stable visible light responding photocatalytic performance of hybrid iodoargentate should be attributed to the combination effect of optical active organic cation and iodoargentate network. On the one hand, the introduction of conjugated organic cations leads to the narrow band gap of hybrid iodoargentate than β-AgI. On the other hand, the photoinduced electrons are able to easily transfer to the conjugated organic cations leading to the stability of hybrid iodoargentate under visible light irradiation. Further studies on the structural regulation and structure–photocatalytic property relationship are in progress in our group.

Acknowledgments

We thank the financial supports from the National Nature Science Foundation of China (Nos. 21201081 and 21571081) and Fund of state key laboratory of structural chemistry (No. 20150005). We also thank Prof. Jiang-Gao Mao at FJIRSM for help with the electronic structure calculation.

Supplementary Information

Electronic supplementary information (ESI) available: Crystallographic data in CIF format (CCDC numbers 1418709 for **1**, 1418706 for **2**, 1418710 for **3** and 1418711 for **4**), tables of selected bonds, luminescent, TGA, photodegradation curves and XRD powder patterns.

REFERENCES

1 (*a*) C. Bellitto, E. M. Bauer, G. Righini, *Coord. Chem, Rev*., 2015, **289-290**, 123−136; (*b*) Y. Takahashi, R. Obara, K. Nakagawa, M. Nakano, J. Tokita, T. Inabe, *Chem*. *Mater*., 2007, **19**, 6312−6316; (*c*) S. P. Zhao, X. M. Ren, *Dalton Trans*., 2011, **40**, 8261-8272; (*d*) R. Peng, M. Li, D. Li, *Coord. Chem*, *Rev*., 2010, **254**, 1−18.

2 (*a*) S. Kazim, M. K. Nazeeruddin, M. Grätzel, S. Ahmad, *Angew. Chem. Int. Ed*., 2014, **53**, 2812−2824; (*b*) F. Hao, C. C. Stoumpos, R. P. H. Chang, M. G. Kanatzidis, *J. Am. Chem. Soc*., 2014, **136**, 8094−8099; (*c*) P. Gao, M. Grätzel, M. K. Nazeeruddin, *Energy Environ*. *Sci*., 2014, **7**, 2448−2463; (*d*) C. C. Stoumpos, L. Frazer, D. J. Clark, Y. S. Kim, S. H. Rhim, A. J. Freeman, J. B. Ketterson, J. I. Jang, M. G. Kanatzidis, *J. Am. Chem. Soc*., 2015, **137**, 6804−6819.

3 (a) Z. J. Zhang, S. C. Xiang, G. C. Guo, G. Xu, M. S. Wang, J. P. Zou, S. P. Guo, J. S. Huang, *Angew. Chem. Int. Ed*., 2008, **47**, 4149−4152; (*b*) Z. J. Zhang, G. C. Guo, G. Xu, M. L. Fu, J. P. Zou, Huang, J. S. *Inorg. Chem*., 2006, **45**, 10028−10030; (*c*) R. G. Lin, G. Xu, G. Lu, M. S. Wang, P. X. Li, G. C. Guo, *Inorg*. *Chem*., 2014, **53**, 5538−5545; (*d*) S. Sourisseau, N. Louvain, W. H. Bi, N. Mercier, D. Rondeau, J. Y. Buzaré, C. Legein, *Inorg. Chem*., 2007, **46**, 6148−6154.

4 (*a*) S. A. Adonin, M. N. Sokolov, A. I. Smolentsev, S. G. Kozlova, V. P. Fedina, *Dalton Trans*., 2013, **42**, 9818−9821; (*b*) K. Y. Monakhov, C. Gourlaouen, R. Pattacini, P. Braunstein, *Inorg*. *Che*m., 2012, **51**, 1562−1568; (*c*) N. Leblanc, M. Allain, N. Mercier, E. Cariati, *Cryst*. *Growth Des*., 2011, **11**,

5200−5205; (*d*) N. Leblanc, N. Mercier, L. Zorina, S. Simonov, P. Auban-Senzier, C. Pasquier, *J. Am. Chem. Soc*., 2011, **133**, 14924−14927.

5 (*a*) A. M. Goforth, M. A. Tershansy, M. D. Smith, L. P. Jr., J. G. Kelley, W. J. I. DeBenedetti, H.-C. Z. Loye, *J. Am. Chem. Soc*., 2011, **133**, 603−612; (*b*) J. P. Li, L. H. Li, L. M. Wu, L. Chen, *Inorg. Chem*., 2009, **48**, 1260−1262; (*c*) Y. Chen, Z. Yang, C. X. Guo, C. Y. Ni, H. X. Li, Z. G. Ren, J. P. Lang, *CrystEngComm*, 2011, **13**, 243−250.

6 (*a*) S. Mishra, E. Jeanneau, G. Ledoux, S. Daniele, *Inorg. Chem*., 2014, **53**, 11721−11731; (*b*) D. H. Cao, C. C. Stoumpos, O. K. Farha, J. T. Hupp, M. G. Kanatzidis, *J. Am. Chem. Soc*., 2015, **137**, 7843−7850; (*c*) Z. T. Xu, D. B. Mitzi, D. R. Medeiros, *Inorg. Chem*., 2003, **42**, 1400−1402; (*d*) E. R. Dohner, E. T. Hoke, H. I. Karunadasa, *J. Am. Chem. Soc*., 2014, **136**, 1718−1721.

7 (*a*) S. Mishra, E. Jeanneau, G. Ledoux, S. Daniele, *Inorg. Chem*., 2014, **53**, 11721−11731; (*b*) H. H. Li, Y. Y. Xing, Z. X. Lian, A. W. Gong, H. Y. Wu, Y. Li, Z. R. Chen, *CrystEngComm*, 2013, **15**, 1721−1728.

8 C. Y. Yue, C. F. Yan, R. Feng, M. Y. Wu, L. Chen, F. L. Jiang, M. C. Hong, *Inorg. Chem*., 2009, **48**, 2873−2879.

9 (*a*) G. C. Xiao, *J. Cluster Sci*. 2006, **17**, 457−466; (*b*) H. H. Li, J. B. Li, M. Wang, S. W. Huang, Z. R. Chen, *J. Cluster Sci*., 2011, **22**, 573−586.

10 (*a*) Y. B. Lu, L. Z. Cai, J. P. Zou, X. Liu, G. C. Guo, J. S. Huang, *CrystEngComm*, 2011, **13**, 5724-5729; (*b*) W. X. Xu, W. X. Zhou, J. Li, S. L. Huang, J. Niu, F. X. Zhang, *Inorg. Chem. Commun*., 2014, **40**, 220-222; (*c*) T. L. Yu, J. J. Shen, Y. B. Fu, Y. L. Fu, *CrystEngComm*, 2014, **16**, 5280-5289.

11 (*a*) G. N. Liu, L. L. Liu, Y. N. Chu, Y. Q. Sun, Z. W. Zhang, C. C. Li, *Eur. J. Inorg. Chem*., 2015, 478−487; (*b*) Y. Z. Qiao, W. Z. Fu, J. M. Yue, X. C. Liu, Y. Y. Niu, H. W. Hou, *CrystEngComm*,

2012, **14**, 3241−3249; (*c*) L. Li, H. Chen, Y. Z. Qiao, Y. Y. Niu, *Inorg. Chem. Acta*, 2014, **409**, 227−232.

12 (*a*) H. H. Li, Z. R. Chen, L. C. Cheng, M. Feng, H. D. Zheng, J. Q. Li, *Dalton Trans*., 2009, 4888−4895; (*b*) H. H. Li, J. X. Wu, H. J. Dong, Y. L. Wu, Z. R. Chen, *J. Mol. Struct*., 2011, **987**, 180−185; (*c*) H. H. Li, S. W. Huang, Z. X. Lian, J. B. Liu, M. Wang, Z. R. Chen, *Z. Anorg. Allg. Chem*. 2012, **638**, 851–855; (*d*) W. Fang, C. Y. Tang, R. H. Chen, D. X. Jia, W. Q. Jiang, Y. Zhang, *Dalton Trans*., 2013, **42**, 15150−15158.

13 J. F. Bringley, M. Rajeswaran, L. P. Olson, N. M. Liebert, *J. Solid State Chem*., 2005, **178**, 3074−3089.

14 (*a*) G. Helgesson, S. Jagner, *J. Chem. Soc., Dalton Trans*., 1990, 2413−2420; (*b*) C. J. Gilmore, P. A. Tucker, P. Woodward, *J. Chem. Soc. A*., 1971, 1337−1341.

15 (*a*) R. C. Zhang, Y. J. Zhang, B. Q. Yuan, J. P. Miao, B. H. Pei, P. P. Liu, J. J. Wang, D. J. Zhang, *J. Solid State Chem*., 2014, **220**, 185−190; (*b*) J. M. Yue, Y. Y. Niu, B. Zhang, S. W. Ng, H. W. Hou, *CrystEngComm*, 2011, **12**, 2571−2577.

16 (*a*) H. H. Li, Z. R. Chen, J. Q. Li, C. C. Huang, Y. F. Zhang, G. X. Jia, *Eur. J. Inorg. Chem*., 2006, 2447−2453; (*b*) H. H. Li, Z. R. Chen, J. Q. Li, C. C. Huang, Y. F. Zhang, G. X. Jia, *Cryst. Growth Des*., 2006, **6**, 1813−1820.

17 Q. Y. Chen, X. Cheng, T. Wang, Z. H. Yu, C. Zhang, S. K. Lin, H. H. Li, Z. R. Chen, *Z. Anorg. Allg. Chem*., 2014, **640**, 439−443.

18 (*a*) T. L. Yu, L. An, L. Zhang, J. J. Shen, Y. B. Fu, Y. L. Fu, *Cryst. Growth Des*., 2014, **14**, 3875−3879; (*b*) E. Cariati, R. Macchi, D. Roberto, R. Ugo, S. Galli, N. Masciocchi, A. Sironi, *Chem. Mater.*, 2007, **19***,* 3704−3711.

19 J. J. Shen, C. F. Zhang, T. L. Yu, L. An, Y. L. Fu, *Cryst. Growth Des*., 2014, **14**, 6337−6342.

20 (*a*) Y. S. Jiang, H. G. Yao, S. H. Ji, M. Ji, Y. L. An, *Inorg. Chem*., 2008, **47**, 3922−3924; (*b*) H. H. Li, Z. R. Chen, L. G. Sun, Z. X. Lian, X. B. Chen, J. B. Li, J. Q. Li, *Cryst. Growth Des*., 2010, **10**, 1068−1073; (*c*) Y. L. Shen, J. L. Lu, C. Y. Tang, W. Fang, Y. Zhang, D. X. Jia, *RSC Adv*., 2014, **4**, 39596−39605.

21 (*a*) S. Mishra, E. Jeanneau, G. Ledoux, S. Daniele, *Dalton Trans*. 2009, 4954−4961; (*b*) S. Mishra, E. Jeanneau, S. Daniele, G. Ledoux, *Dalton Trans*., 2008, 6296−6304.

22 (a) R. Asahi, T. Morikawa, T. Ohwaki, K. Aoki, Y. Taga, *Science*, 2001, **293**, 269-271; (b) K. Maeda, Y. Shimodaira, B. Lee, K. Teramura, D. Lu, H. Kobayashi, K. Domen, *J. Phys. Chem. C*, 2007, **111**, 18264–18270.

23 G. M. Sheldrick, SHELXTL, University of Götingen, Götingen, 2001.

24 (*a*) M. D. Segall, P. J. D. Lindan, M. J. Probert, C. J. Pickard, P. J. Hasnip, S. J. Clark, M. C. Payne, *J. Phys.: Condens. Matter*., 2002, **14**, 2717−2744; (*b*) V. Milman, B. Winkler, J. A. White, C. J. Pickard, M. C. Payne, E. V. Akhmatskaya, R. H. Nobes, *Int. J. Quantum Chem*., 2000, **77**, 895−910; (*c*) J. P. Perdew, K. Burke, M. Ernzerhof, *Phys. Rev. Lett*. 1996, **77**, 3865−3868.

25 (*a*) C. Y. Yue, Z. D. Yuan, L. G. Zhang, Y. B. Wang, G. D. Liu, L. K. Gong, X. W. Lei, *J. Solid State. Chem*. 2013, **206**, 129-133; (*b*) C. Y. Yue, X. W. Lei, H. P. Zang, X. R. Zhai, L. J. Feng, Z. F. Zhao, J. Q. Zhao, X. Y. Liu, *CrystEngComm*. 2014, **16**, 3424-3430; (*c*) C. Y. Yue, X. W. Lei, Y. X. Ma, N. Sheng, Y. D. Yang, G. D. Liu, X. R. Zhai, *Cryst. Growth Des*. 2014, **14**, 101-109.

26 (*a*) C. Y. Yue, X. W. Lei, L. Yin, X. R. Zhai, Z. R. Ba, Y. Q. Niu, Y. P. Li, *CrystEngComm*. 2015, **17**, 814-823; (*b*) C. Y. Yue, X. W. Lei, L. J. Feng, C. Wang, Y. P. Gong, X. Y. Liu, *Dalton Trans*. 2015, **44**, 2416-2424; (*c*) C. Y. Yue, X. W. Lei, R. Q. Liu, H. P. Zhang, X. R. Zhai, W. P. Li, M. Zhou, Z. F. Zhao, Y. X. Ma, Y. D. Yang, *Cryst. Growth Des*. 2014, **14**, 2411-2421.

27 H. Paulsson, M. Berggrund, A. Fischer, L. Kloo, *Eur. J. Inorg. Chem*., 2003, 2352−2355.

28 S. L. Li, X. M. Zhang, *Inorg. Chem*., 2014, **53**, 8376−8383.

29 A. Bondi, *J. Phys. Chem*., 1964, **68**, 441−451.

30 M. Henary, J. I. Zink, *Inorg. Chem*., 1991, **30**, 3111−3112.

31 (*a*) P. Wang, B. B. Huang, X. Y. Qin, X. Y. Zhang, Y. Dai, J. Y. Wei, M. H. Whangbo, *Angew. Chem., Int. Ed*., 2008, **47**, 7931−7933; (*b*) Y. X. Tang, Z. L. Jiang, G. C. Xing, A. R. Li, P. D. Kanhere, Y. Y. Zhang, T. C. Sum, S. Z. Li, X. D. Chen, Z. L. Chen, Z. Chen, *Adv. Funct. Mater.*, 2013, **23**, 2932−2940; (*c*) C. H. An, S. Peng, Y. G. Sun, *Adv. Mater.*, 2010, **22**, 2570−2574.

32 (*a*) S. S. Soni, M. J. Henderson, J. F. Bardeau, A. Gibaud, *Adv. Mater*., 2008, **20**, 1493−1498; (*b*) M. R. Hoffmann, S. T. Martin, W. Choi, W. Bahnemann, *Chem. Rev*., 1995, **95**, 69−96.

33 (*a*) T. L. Yu, Y. B. Fu, Y. L. Wang, P. F. Hao, J. J. Shen, Y. L. Fu, *CrystEngComm*, 2015, DOI: 10.1039/C5CE01692D; (*b*) T. L. Yu, J. J. Shen, Y. L. Wang, Y. L. Fu, *Eur. J. Inorg. Chem*. 2015, 1989−1996; (*c*) X. W. Lei, C. Y. Yue, J. Q. Zhao, H. F. Han, J. T. Yang, R. R. Meng, C. S. Gao, H. Ding, C. Y. Wang, W. D. Chen, M. C. Hong, *Inorg. Chem*. 2015, DOI: 10.1021/acs.inorgchem.5b01324; (*d*) X. W. Lei, C. Y. Yue, J. Q. Zhao, Y. F. Han, J. T. Yang, R. R. Meng, C. S. Gao, H. Ding, C. Y. Wang, W. D. Chen, *Cryst. Growth Des*., 2015, DOI: 10.1021/acs.cgd.5b01037.

Captions for figures

Fig. **1**. Ball-and-stick representations of $[Ag_3I_7]^{4-}$ unit (a) as well as the packing arrangement along the *c*-axis (b), and the structure of compound **1** along the *b*-axis (c).

Fig. **2**. Detailed view of the $[Ag_3I_7]$ trimer (a), $[Ag_7I_{13}]$ unit (b), 2D $[Ag_5I_7]^{2-}$ layer (c) and the stacking structure of compound **2** along *a*-axis (d). The green and red mode represents the $[Ag_3I_7]$ and $[Ag_7I_{13}]$ unit, respectively, one for clarity.

Fig. **3**. The formation schema of 2D $[Ag_{14}I_{22}]^{8-}$ layer (a) and view of the structure of compound **4** along the *a*-axis (b).

Fig. **4**. Solid-state optical absorption spectrum of compounds **1**-**4**.

Fig. **5**. Absorption spectra of the solution of CV (a) and RhB (c) in the presence of sample **4** under the visible light irradiation, photodegradation ratios of CV (b) and RhB (d) by sample **4** monitored as the normalized change in concentration as function of irradiation time.

Fig. **6**. Total and partial DOS of compound **4**.

Table 1. Crystal Data and Structure Refinements for compounds **1-4**.

Compound	**1**	**2**	**3**	**4**
Chemical Formula	$C_{72}N_{12}H_{48}Mn_2Ag_3I_7$	$C_{72}N_{12}H_{48}Fe_2Ag_3I_7$	$C_{36}N_6H_{24}MnAg_5I_7$	$C_{24}N_4H_{28}Ag_7I_{11}$
FW	2403.01	2404.83	2023.20	2523.49
Space group	*R*-3*c* (No. 167)	*R*-3*c* (No. 167)	*P*-1 (No. 2)	*P*-1 (No. 2)
a/Å	15.1789(4)	15.1612(16)	14.7523(14)	11.3960(14)
b/Å	15.1789(4)	15.1612(16)	14.7794(14)	18.948(2)
c/Å	58.192(4)	58.187(9)	27.291(3)	23.015(3)
$\alpha/^o$	90	90	76.7800(10)	100.4410(10)
$\beta/^o$	90	90	86.8430(10)	94.9510(10)
$\gamma/^o$	120	120	60.3180(10)	100.2270(10)
V(Å^3)	11611.1(9)	11583(3)	5020.6(8)	4773.6(10)
Z	6	6	4	2
D_{calcd} (g·cm^{-3})	2.062	2.069	2.677	3.511
Temp (K)	293(2)	293(2)	293(2)	293(2)
μ (mm^{-1})	3.903	2.069	6.491	9.948
F(000)	6755	6768	3652	4448
Reflections collected	25579	28574	57677	56436
Unique reflections	2959	2933	22542	21694
Reflections ($I>2\sigma(I)$)	2688	2702	14925	15857
GOF on F^2	1.055	1.068	1.045	1.023
R_1, wR_2 ($I > 2\sigma(I)$)[a]	0.0435/0.1445	0.0375/0.1486	0.0520/0.1453	0.0399
R_1, wR_2 (all data)	0.0483/0.1493	0.0403/0.1518	0.0883/0.1623	0.0915
$\Delta\rho_{max}$ (e/Å^3)	1.687	1.882	2.979	2.884
$\Delta\rho_{min}$ (e/Å^3)	-1.282	-1.367	-1.936	-2.356

[a] $R_1 = \sum||F_o| - |F_c||/\sum|F_o|$, $wR_2 = \{\sum w[(F_o)^2 - (F_c)^2]^2/\sum w[(F_o)^2]^2\}^{1/2}$

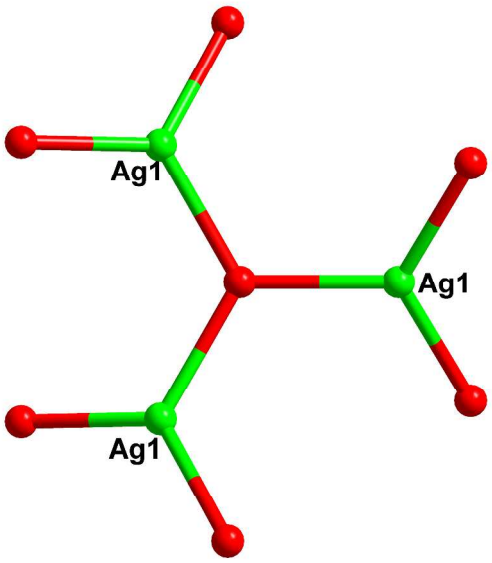

1323x991mm (96 x 96 DPI)

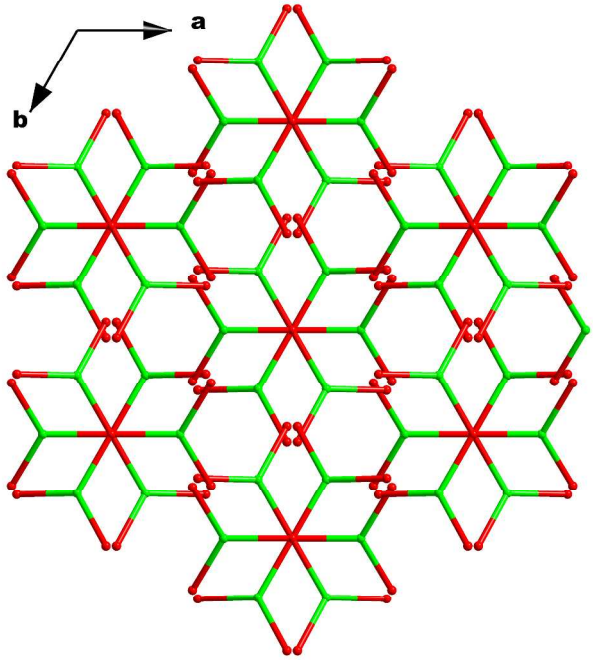

1323x991mm (96 x 96 DPI)

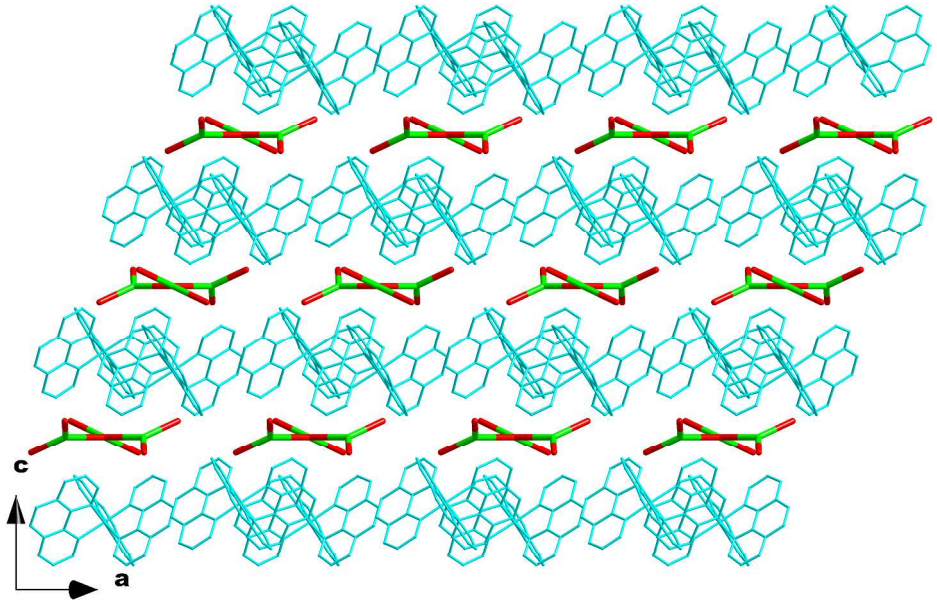

1323x991mm (96 x 96 DPI)

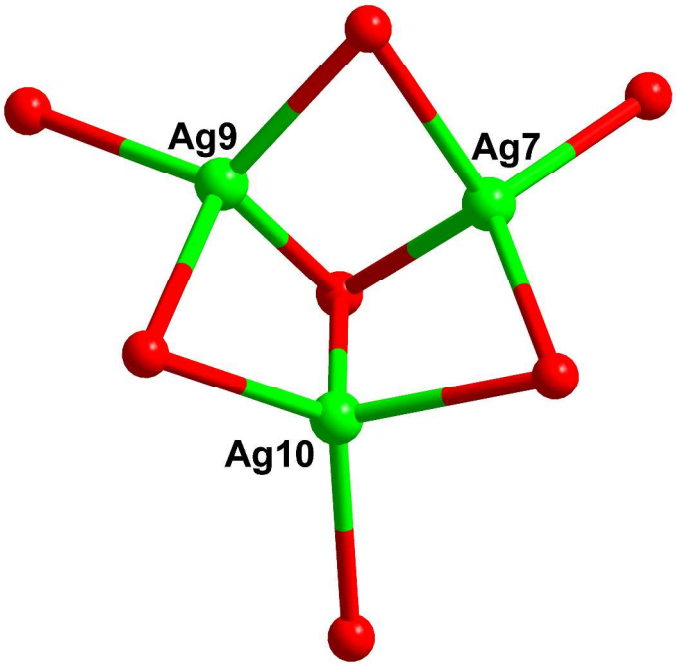

1323x991mm (96 x 96 DPI)

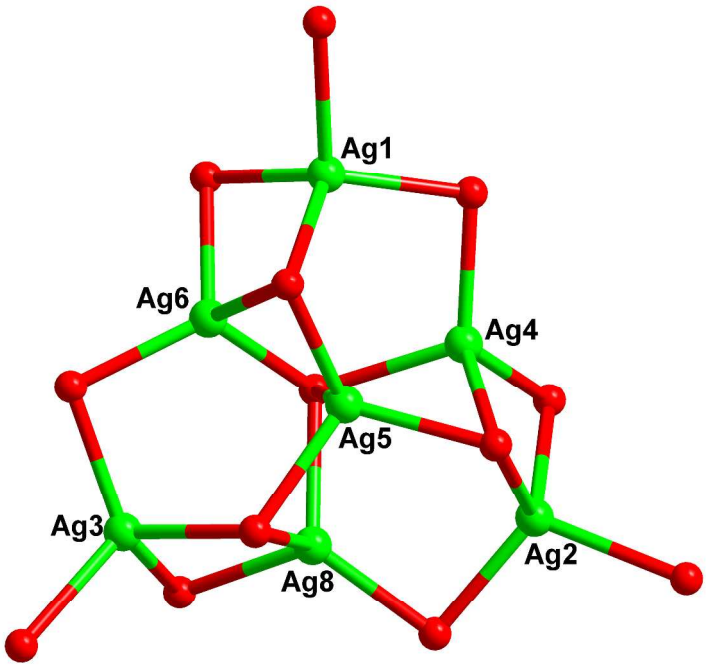

1323x991mm (96 x 96 DPI)

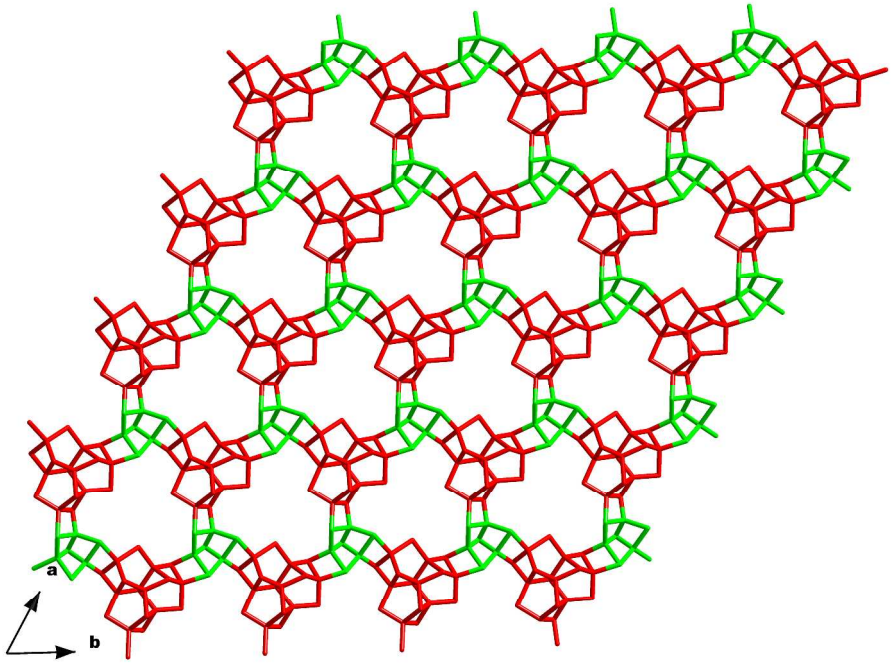

1323x991mm (96 x 96 DPI)

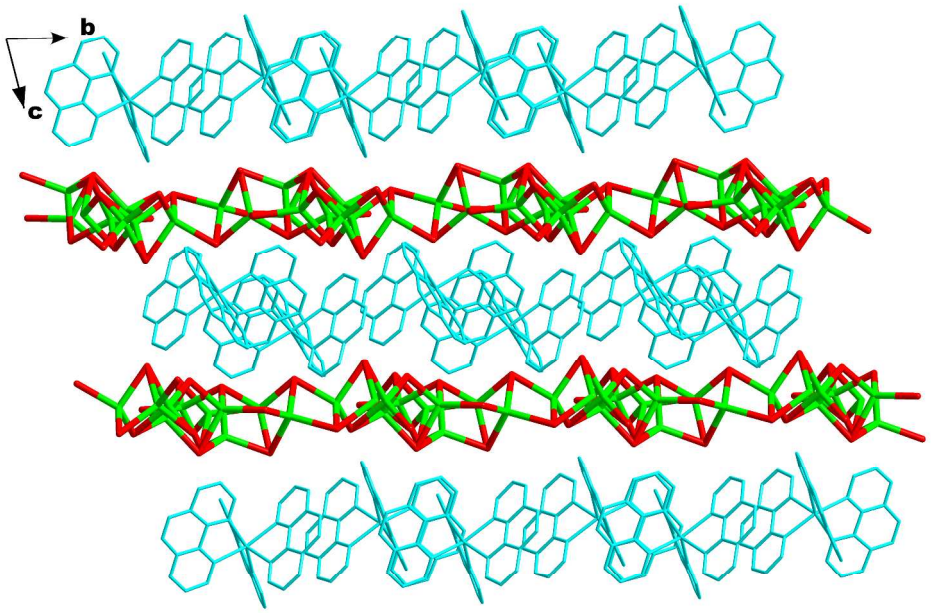

1323x991mm (96 x 96 DPI)

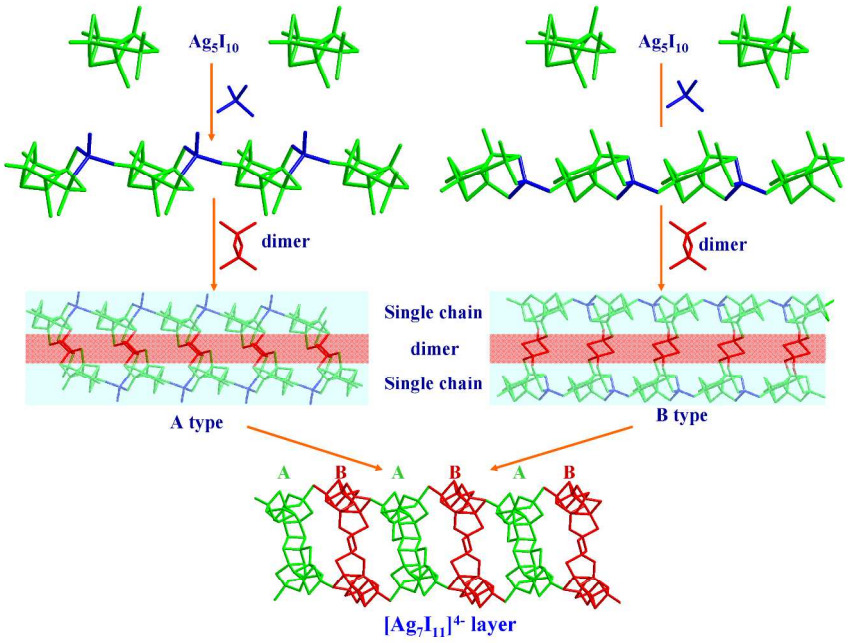

297x209mm (300 x 300 DPI)

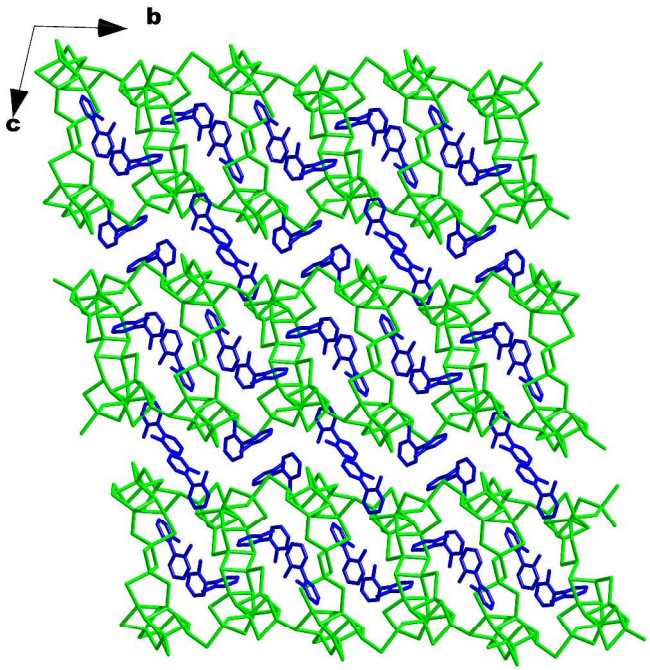

1323x991mm (96 x 96 DPI)

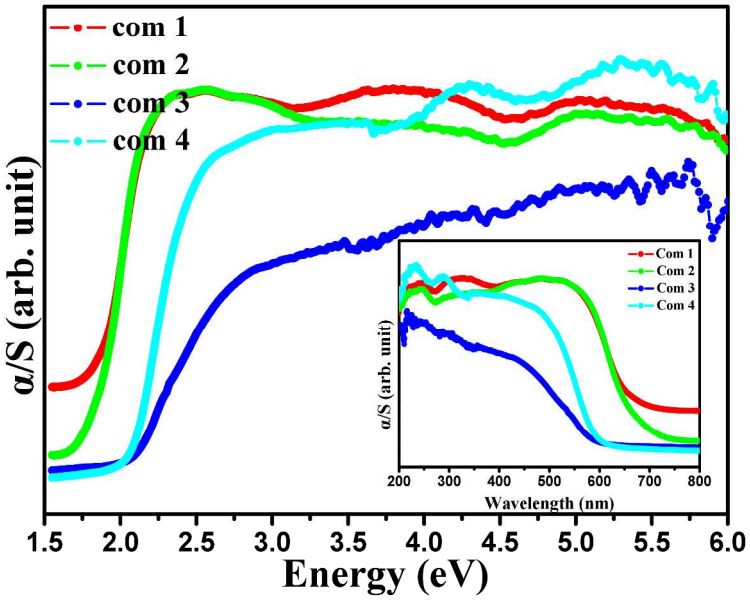

297x209mm (300 x 300 DPI)

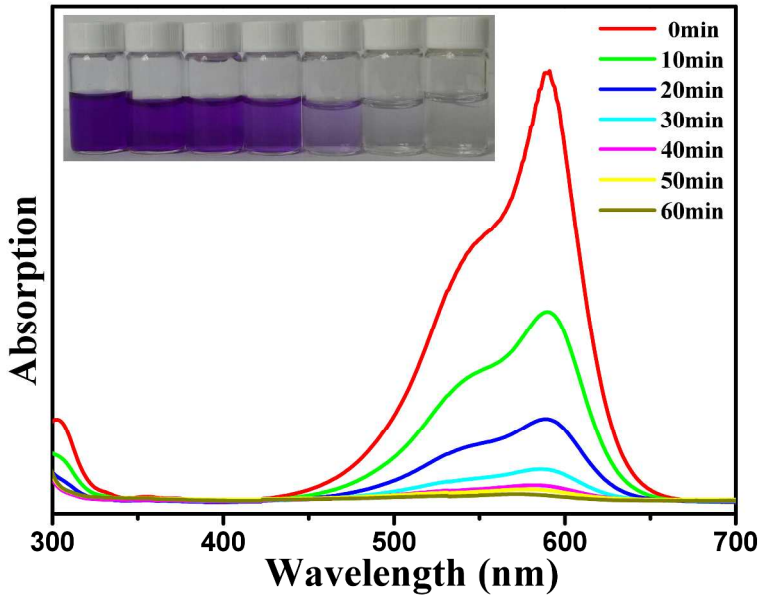

297x209mm (300 x 300 DPI)

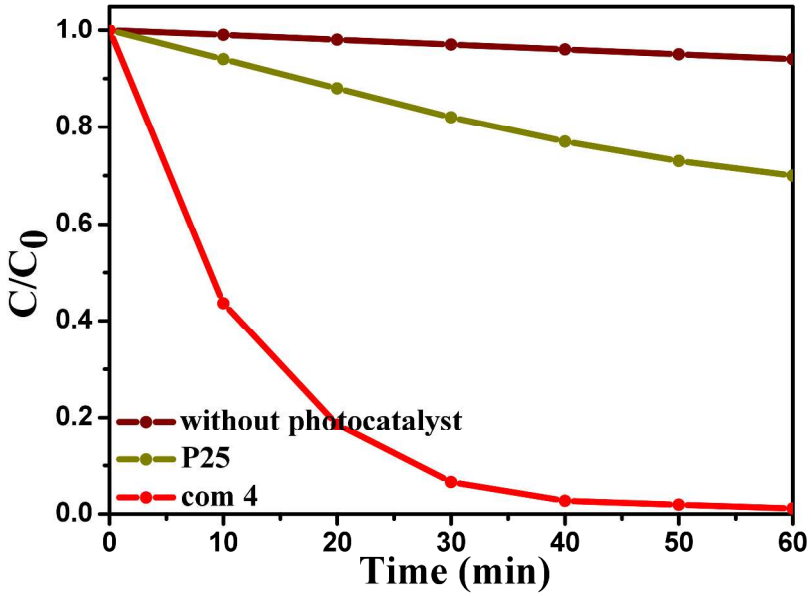

297x209mm (300 x 300 DPI)

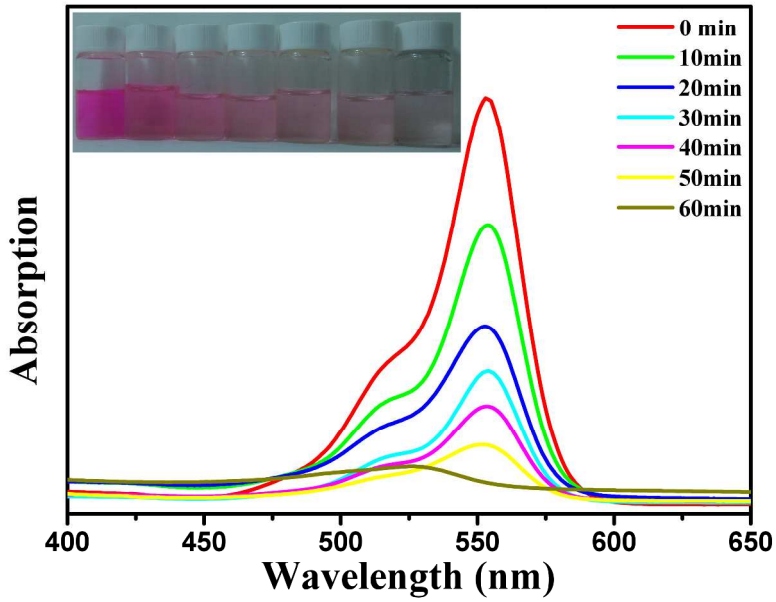

297x209mm (300 x 300 DPI)

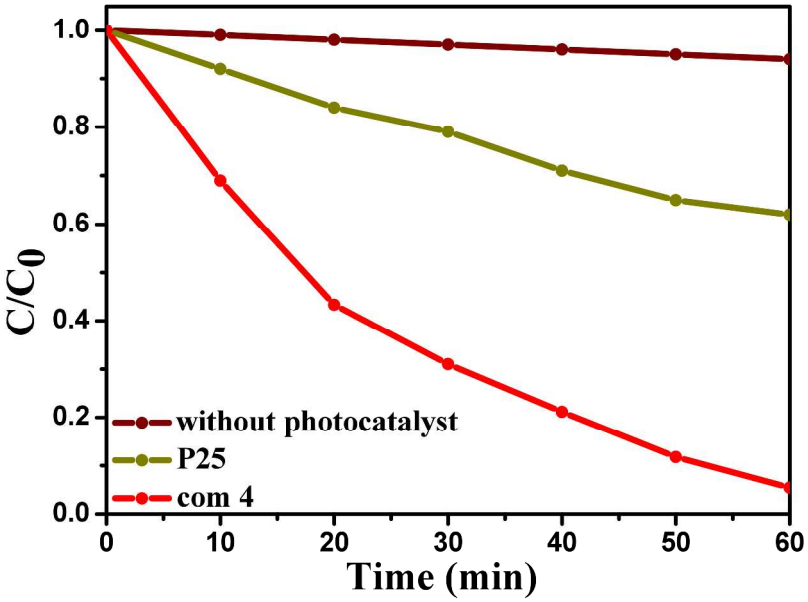

297x209mm (300 x 300 DPI)

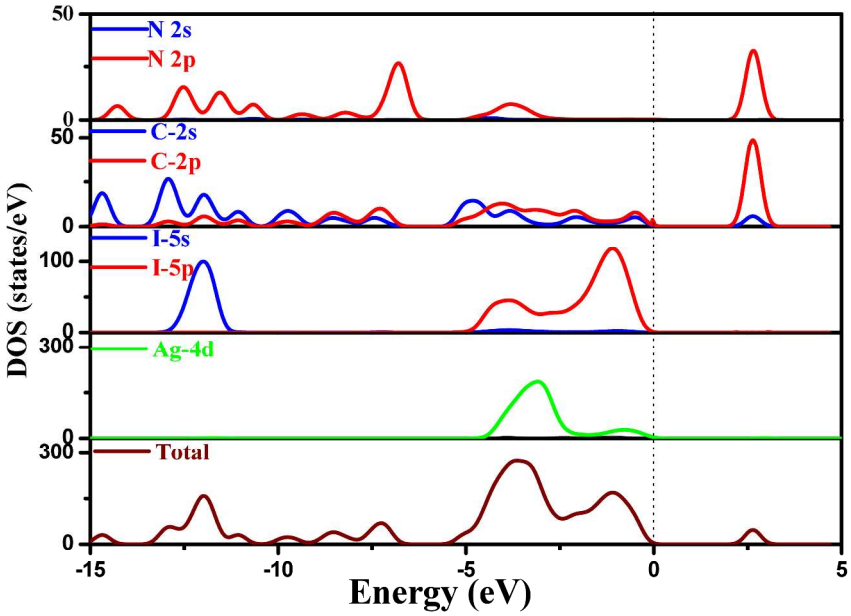

297x209mm (300 x 300 DPI)